ELSEVIER

Contents lists available at ScienceDirect

# Journal of Materials Research and Technology

journal homepage: www.elsevier.com/locate/jmrt





# Finite Element modeling of the carburizing-quenching process in steels

Salim Ben Ayed a,b,c,\* , Yann Charles a, Laurent Daniel b,c

- <sup>a</sup> Université Sorbonne Paris Nord, Laboratoire des Sciences des Procédés et des Matériaux, LSPM, CNRS, UPR 3407, F-93430, Villetaneuse, France
- b Université Paris-Saclay, CentraleSupélec, CNRS, Laboratoire de Génie Electrique et Electronique de Paris, F-91192, Gif-sur-Yvette, France
- <sup>c</sup> Sorbonne Université, CNRS, Laboratoire de Génie Electrique et Electronique de Paris, F-75252, Paris, France

#### ARTICLE INFO

Handling Editor: SN Monteiro

Keywords:
Carburization
Quenching
Martensitic transformation
Transformation plasticity
Diffusion
Internal stresses
Surface hardness
Abaqus
User subroutine

#### ABSTRACT

Carburizing-quenching is a thermochemical surface treatment designed to harden the surface of steels and make them more resistant to friction, wear, and corrosion. It involves the diffusion of carbon atoms at high temperature, followed by rapid cooling to induce a phase transformation from austenite to martensite. This process therefore combines a diffusion process, possibly assisted by stress fields, a heat transfer process, and metallurgical transformations, which interact and induce residual stresses, linked to various deformations connected to the coupled processes involved.

The objective of this work is to develop a finite element model to capture these residual stresses, together with composition gradients in the material. This model, based on the Abaqus finite element software, relies on numerous user subroutine, allowing the highly coupled resolution of the physics associated with carburizing-quenching. This model is applied to a simple structure inspired by previous works in the literature, the results highlight that mechanical fields have a significant influence on both diffusion and residual stress profiles, particularly near the surface. Neglecting these effects can lead to substantial errors in the prediction of local composition and mechanical performance.

# 1. Introduction

Carburizing followed by quenching is one of the oldest heat treatments used to harden surfaces. This process is particularly effective in producing steels with wear-resistant surfaces, capable of enduring high stresses, deformations, fatigue and corrosion. This improvement in surface performance is beneficial for various machine parts such as gears and bearings, used in a wide range of sectors including automotive and aerospace [1].

The carburizing-quenching process takes place in three successive steps (see Fig. 1), which can be repeated. The first step is the heating of the part in a carburizing furnace [3] until it reaches a uniform temperature and a homogeneous austenitic state. The second step is the diffusion of carbon atoms from the surface, which creates a concentration gradient. The third and final step is quenching. This stage involves rapid cooling of the carburized part to obtain a martensitic microstructure, which plays a major role in the final mechanical properties. Martensite exhibits high strength and hardness [4], and the martensitic transformation generates residual compressive stresses at the surface, which are beneficial to the mechanical properties. However, tensile stresses are

also present within the sample volume [5], which must be controlled carefully.

The coupling between the mechanisms involved appears at different levels (see Fig. 2): the diffusion process drives the carbon-concentration profile; phase transformations are driven by temperature evolution and carbon-concentration; temperature fields are influenced by phase transformation; thermal stresses impact the mechanical response. Last, phase transformations are associated to transformation strains that can generate transformation plasticity [6]. Stresses can influence the kinetics of the martensitic transformation.

Many studies have been conducted in the literature, using Finite Element (FE) tools, to investigate the impact of carburizing and heat treatments on material properties (e.g., hardness, composition ...); a broad (although not exhaustive) survey was carried out and summarized in the Appendix, highlighting the relevance of the developments presented in the current study. This leads to the combination of several problems, especially related to species diffusion, heat transfer, plasticity, and phase transformation. The classical scenario consists in two stages:

E-mail address: salim.ben-ayed@lspm.cnrs.fr (S. Ben Ayed).

<sup>\*</sup> Corresponding author. Université Sorbonne Paris Nord, Laboratoire des Sciences des Procédés et des Matériaux, LSPM, CNRS, UPR 3407, F-93430, Villetaneuse, France.

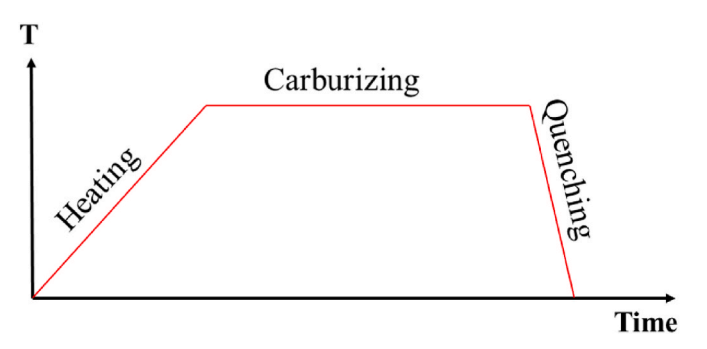


Fig. 1. Temperature profile for the carburizing - quenching process [2].

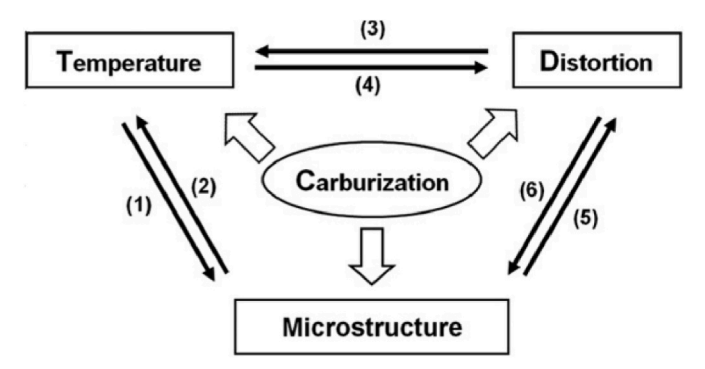


Fig. 2. Interactions during the carburizing-quenching treatment [7].

- Carburizing: species diffusion at a given elevated temperature, assumed to be constant throughout the process;
- 2. Quenching, along with phase transformations and plasticity.

In step 2, as temperature variations are fast (especially with respect to species diffusion), no diffusion occurs.

The carbon diffusion is based on the Fick law, with a carbon diffusion coefficient D which can be considered as carbon-concentration independent [8–12] or not [13–17]. The impact of stress and strain distribution on diffusion is usually neglected [18].

Heat transfer is usually modelled based on the Fourier's law, in which dissipation heat sources (related to plasticity and phase change) can be considered [5,19,20], as well as thermal expansion.

During quenching, the mechanical behavior combines several contributions: elastoplasticity, transformation plasticity, and transformation strains [12,13]. The impact of viscosity on the mechanical response [21-23], or the contribution of dilatational strain induced by carbon atoms [8] can also be included. It is worth noting that a mechanical resolution is not required if the impact of internal stresses on the quenching mechanisms is neglected [15-17].

Last, phase transformations are usually described using phenomenological approaches, assuming an instantaneous process (i.e., faster than all other phenomena), depending on temperature, carbon-concentration, and stress levels [24,25]. Recent investigations proposed a kinetic model of theses transformations [8,23].

The aim of this work is to model the entire carburizing-hardening process in order to evaluate the chemical composition and internal stresses at the end of the process. This involves especially to be able to couple transient diffusion of carbon and heat (accounting for mechanical fields or not), then to link concentration, temperature and phase change, which will be considered as instantaneous.

The paper is organized as follows: the used models are first presented, as well as the implementation strategy in the commercial FE software Abaqus. Then, an application is carried out on a cylinder loaded following a scenario from the literature [8], in order to evaluate

the distribution of the various physical fields in the structure at the end of the carburizing-quenching process. In this work, two additional contributions are considered compared to most existing models: (i) the influence of hydrostatic stress on carbon diffusion [18,28], and (ii) the volumetric deformation induced by carbon atoms [8]. These effects, never considered simultaneously in the literature, are expected to have an impact on the prediction of residual stress distributions and carbon concentration profiles. Unless specified otherwise, all concentrations are expressed in weight percent (wt.%).

## 2. Modeling

The coupled problem described in Fig. 2 has been implemented in Abaqus software [26] using several User Subroutines [27]. The different models considered are first presented, followed by a description of the implementation process. The phase transformation kinetics is neglected here, and only two phases are considered: austenite and martensite.

#### 2.1. Heat transfer

The classical Heat transfer equation has been used [28], such that the temperature gradient  $\nabla T$  is linked to the heat flux  $\varphi$ 

$$\varphi = -k\nabla T \tag{1}$$

where k is the material's thermal conductivity, leading to the following heat transfer equation

$$\rho C_p \dot{T} = \nabla \cdot (k \nabla T) \tag{2}$$

 $\rho$  and  $C_p$  represent the density and the specific heat, respectively, and  $\dot{T}$  denotes the time derivative of T.

The temperature variation induces an isotropic dilatational strain  $\varepsilon^T$ , such that

$$\boldsymbol{\varepsilon}^T = \alpha \Delta T \boldsymbol{I} \tag{3}$$

in which  $\alpha$  is the material's thermal expansion coefficient.  $\Delta T$  is the difference between the current and the initial temperature, and I the identity second order tensor.

No heat dissipation is considered, as it is assumed that its impact on the thermal field is negligible.

## 2.2. Transport of carbon atoms

Carbon atoms transport is modelled using the Fick's first law [3,6], in which the particle's flux J is a function of both carbon-concentration C and hydrostatic pressure gradient  $P_H$  [29]

$$J = -D\nabla C - \frac{DV_c}{RT}C\nabla P_H \tag{4}$$

where  $V_c$  is the partial carbon molar volume, D the diffusion coefficient, R the perfect gas constant.  $P_H = -1/3$  tr  $\sigma$  is the hydrostatic pressure,  $\sigma$  being the stress tensor. The diffusion coefficient D is modelled by an Arrhenius function [30]

$$D = D_0 \exp\left(-\frac{Q}{RT}\right) \tag{5}$$

Q is the activation energy and  $D_0$  is the pre-exponential factor. Both are assumed to be composition-dependent such that [31]

$$\begin{cases} D_0 = 0.146 - 0.036C(1 - 1.075Cr) - 0.0315Mn + 0.0509Si \\ -0.0085Ni + 0.3031Mo - 0.052Al \\ Q = 144300 - 15000C - 370C^2 - 4366.3Mn + 4050.7Si \\ -1240.7Ni + 7726Cr + 12126.6Mo - 6788.6Al \end{cases}$$
(6)

with concentrations in mass percent. Based on mass conservation, the

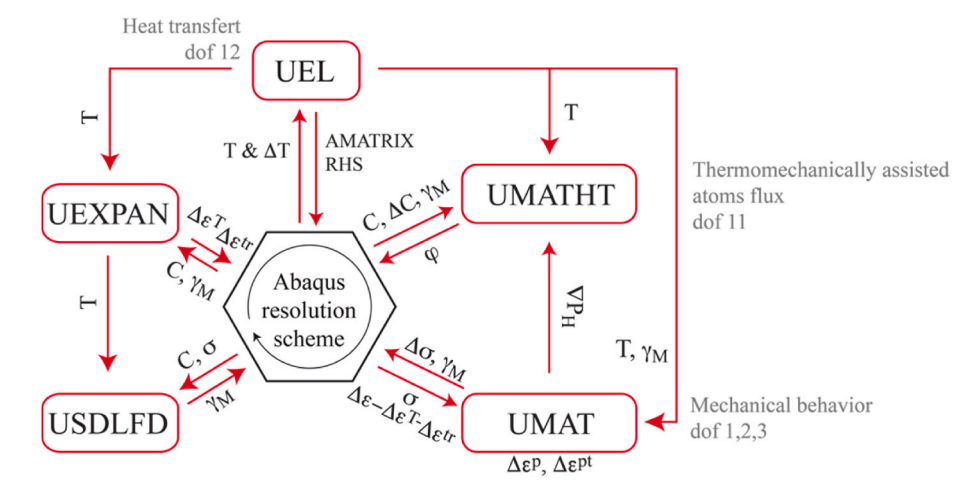


Fig. 3. Flowchart for the resolution of the coupled problem.

Table 1
Composition of the 8620RH steel [8].

	С	Si	Mn	Cr	Ni	P	S	Cu
wt%	0.2	0.27	0.75	0.55	0.55	< 0.035	< 0.035	< 0.3

temporal evolution of C can be deduced:

$$\frac{\partial C}{\partial t} + \operatorname{div} \mathbf{J} = 0 \tag{7}$$

In addition, the diffusion of carbon atoms generates an isotropic dilatational strain  $\epsilon^C$ , such that [8]

$$\boldsymbol{\varepsilon}^{C} = \alpha_{C}(C - C_{0})\boldsymbol{I} \tag{8}$$

in which  $\alpha_C$  is the volume's expansion coefficient due to carbon diffusion and  $C_0$  the initial carbon concentration.

# 2.3. Phase transformation

To model the instantaneous martensite transformation, the martensite volume fraction  $\gamma_M$  is expressed using the Koistinen-Marburger law [32]

$$\gamma_{M} = \gamma_{Ai}[1 - \exp(A_{M}(M_{s} - T))] \tag{9}$$

where  $\gamma_{ai}$  is the initial volume fraction of austenite,  $A_M$  is a dimensionless material parameter [7] such that

$$A_{\rm M} = 0.0231 - 0.0105 \text{C} - 0.0017 \text{Ni} + 0.0074 \text{Cr} - 0.0193 \text{Mo}$$
 (10)

 $M_s$  is the temperature at which martensitic transformation begins, defined by [4]

$$M_s(^{\circ}C) = 500 - 300C - 33Mn - 17Ni - 22Cr - 11Si - 11Mo$$
 (11)

## 2.4. Mechanical behavior

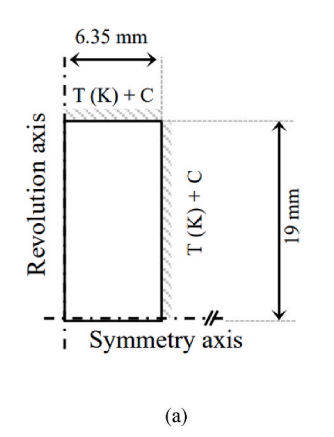
The total strain rate  $\dot{\epsilon}$  is assumed to be divided into several terms (small strain assumption)

$$\dot{\boldsymbol{\varepsilon}} = \dot{\boldsymbol{\varepsilon}}^e + \dot{\boldsymbol{\varepsilon}}^p + \dot{\boldsymbol{\varepsilon}}^T + \dot{\boldsymbol{\varepsilon}}^{tr} + \dot{\boldsymbol{\varepsilon}}^{pt} + \dot{\boldsymbol{\varepsilon}}^C \tag{12}$$

 $\dot{\varepsilon}^e$  and  $\dot{\varepsilon}^p$  are the elastic and plastic strain rates, respectively.  $\dot{\varepsilon}^T$  corresponds to the thermal expansion (equation (3)), and  $\dot{\varepsilon}^C$  to the dilatation induced by the presence of carbon atoms (equation (8)).  $\dot{\varepsilon}^T$ ,

**Table 2** Material parameters: Young Modulus (*E*), Poisson ration ( $\nu$ ) yield stress ( $\sigma_0$ ) [35]. *T* is the temperature in K.

	Austenite	Martensite
E (GPa)	$-6.10^{-5} \times T^2 + 0.0072 \times T + 193.53$	$-3.10^{-5} \times T^2 - 0.048 \times T + 231.84$
ν σ <sub>0</sub> (MPa)	$\begin{array}{c} 2.10^{-8} \times T^2 + 4.10^{-5} \times T + 0.2645 \\ 0.00021 \times T^2 - 0.676 \times T + 514.23 \end{array}$	



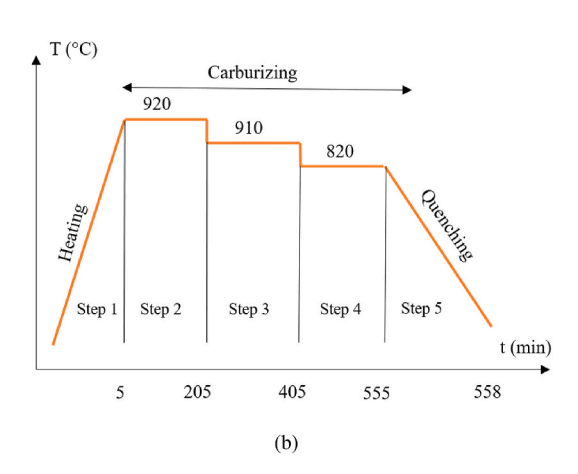


Fig. 4. (a) Dimensions of the sample and (b) And heat treatment process.

Table 3
Heat transfer parameters [20].

<i>T</i> (°C)	$C_p$ (J.kg <sup>-1</sup> .°C <sup>-1</sup> )	$k \text{ (W.m}^{-1}.^{\circ}\text{C}^{-1}\text{)}$	$ ho$ (kg.m $^{-3}$ )
25	0.45	69	7840
100	0.48	64	7824
200	0.52	56	7796
300	0.58	48	7762
400	0.62	43	7728
500	0.71	38	7691
600	0.80	34	7653
700	0.96	32	7615
800	1.01	26	7642
900	0.60	27	7599
1000	0.62	28	7545
1100	0.64	29	7492
1200	0.65	31	7439

the transformation strain rate, corresponds to a volumetric change strain induced by the formation of martensite from austenite: since martensite has a lower lattice parameter than austenite [33], the martensitic transformation results in a relative increase in volume. Last,  $\dot{\epsilon}^{pt}$  is the transformation plasticity strain rate, i.e., the plasticity due to phase transformation.

The elastic strain  $\mathbf{\epsilon}^e$  is related to the stress field by the Hooke's law

$$\varepsilon^{e} = \frac{1+\nu}{E} \sigma - \frac{\nu}{E} \operatorname{tr}(\sigma) I$$
 (13)

where E and  $\nu$  are the Young's modulus and the Poisson's ratio, respectively. Plastic strain is computed based on  $J_2$ -flow theory, using a yield function F such that

$$F = \sigma_{vM} - \sigma_0 - R(p) \tag{14}$$

 $\sigma_{vM}$  is the von Mises stress,  $\sigma_0$  the initial yield stress and R(p) the isotropic hardening term, expressed as  $R(p) = k.p^n$ . p is the cumulated plastic strain, k the hardening coefficient, and n the strain-hardening exponent (respectively set as 500 MPa and 0.5). Plastic strain rate can be computed based on the normality rule [34]

$$\dot{\varepsilon}^p = \dot{p}\frac{\partial F}{\partial \sigma} \tag{15}$$

The transformation strain rate  $\dot{\boldsymbol{\varepsilon}}^{tr}$  can be expressed as follows [5]

$$\dot{\boldsymbol{\varepsilon}}^{tr} = \beta_{M} \dot{\gamma}_{M} \boldsymbol{I} \tag{16}$$

where  $\beta_M$  is the coefficient describing the expansion induced by the structural modifications [19] and  $\gamma_M$  the martensite volume fraction (equation (9)). Last, transformation plasticity strain rate  $\dot{\varepsilon}^{pt}$  is given by [35]

$$\begin{cases} \dot{\epsilon}^{pt} = \frac{3}{2} K s \frac{df}{d\gamma_M} \dot{\gamma}_M \\ f(\gamma_M) = \gamma_M (2 - \gamma_M) \end{cases}$$
 (17)

where K is the material-dependent transformation coefficient, s is the deviatoric stress tensor and  $f(\gamma_{\rm M})$  is a function describing the progression of the transformation. An equivalent transformation plasticity strain  $\varepsilon_{eq}^{pt}$  can be introduced such that

$$\begin{cases} \dot{\varepsilon}_{eq}^{pt} = \sqrt{\frac{2}{3}}\dot{\varepsilon}^{pt} : \dot{\varepsilon}^{pt} = \sqrt{\frac{3}{2}s : s}K \left| \frac{df}{d\gamma_{M}}\dot{\gamma}_{M} \right| = \sigma_{vM}K \left| \frac{df}{d\gamma_{M}}\dot{\gamma}_{M} \right| \\ \varepsilon_{eq}^{pt} = \int_{0}^{t} \dot{\varepsilon}_{eq}^{pt}dt \end{cases}$$
(18)

# 2.5. Implementation

To solve the coupled chemo-thermo-mechanical problem, the Finite Element software Abaqus is used, together with several User Subroutines [27]. The 'coupled-temp' displacement procedure has been used, with the degree of freedom (dof) 11 for the carbon-concentration C.

To add all the specific features presented in the previous sections, the following User Subroutine were used, either from previous developments or specifically designed for that work:

- UMATHT: definition of the pressure-dependent particle flux [36];
- UMAT: thermo-elastoplastic mechanical behavior (isotropic hardening) and computation of ∇P<sub>H</sub> [36]. This subroutine has been modified to account for ε<sup>pt</sup>, using the algorithm presented in [34];
- UEL: multi-diffusion problem [37], and especially, transient heat transfer [38];
- UEXPAN: thermal expansion [38] as well as  $\varepsilon^{tr}$  and  $\varepsilon^{C}$ ;
- USDFLD: computation of  $\gamma_M$  as a function of C and T

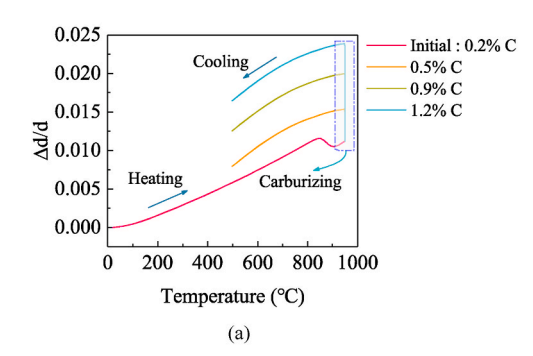
The flowchart is presented in Fig. 3. From the implementation strategy, all material parameters can be dependent on temperature, carbon-concentration and martensite/austenite fraction.

It is worth noting that the chosen implementation strategy allows the resolution of all problems simultaneously, except the phase transformation. As underlined previously, in the specific context of carburizing—quenching, this specificity is not mandatory.

# 3. Application

The model presented in the previous section has been applied on a reference configuration extracted from literature [8], for the sake of illustration, noting that in the current study, only purely martensitic quenching is considered.

First, the geometry and boundary conditions are presented, then the



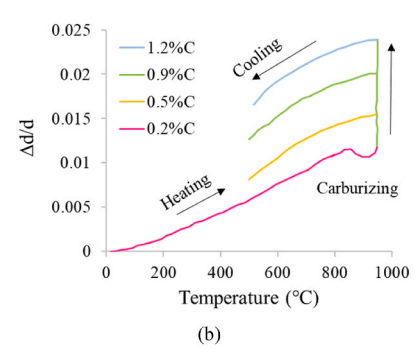


Fig. 5. Variation of the diameter of the sample  $\Delta d/d$  due to both heat transfer and carbon atoms diffusion (a) From [8] and (b) Obtained in the current study after identification of  $\alpha_{\mathbb{C}}$ .

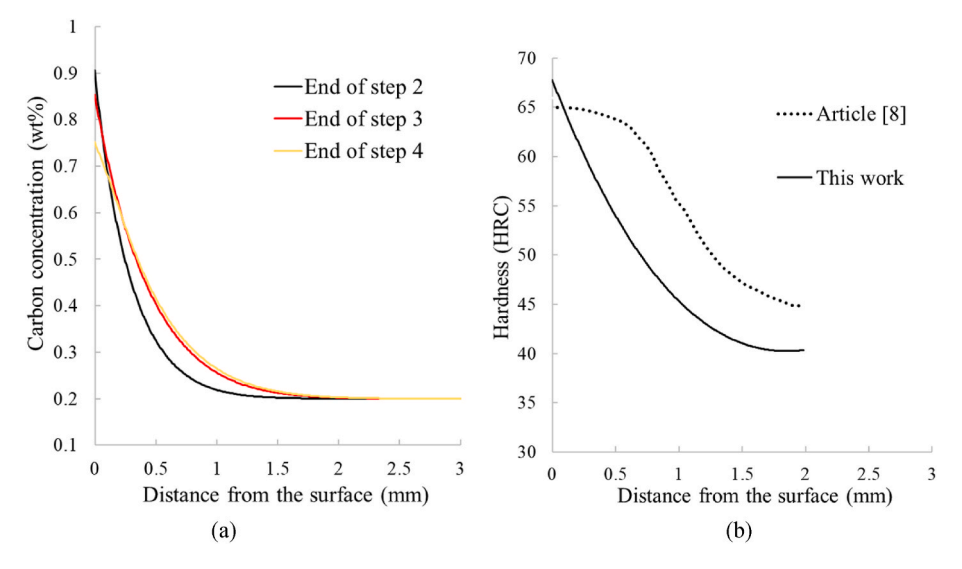


Fig. 6. (a) Carbon penetration in the sample and (b) Comparison of the computed HRC hardnesses with [8].

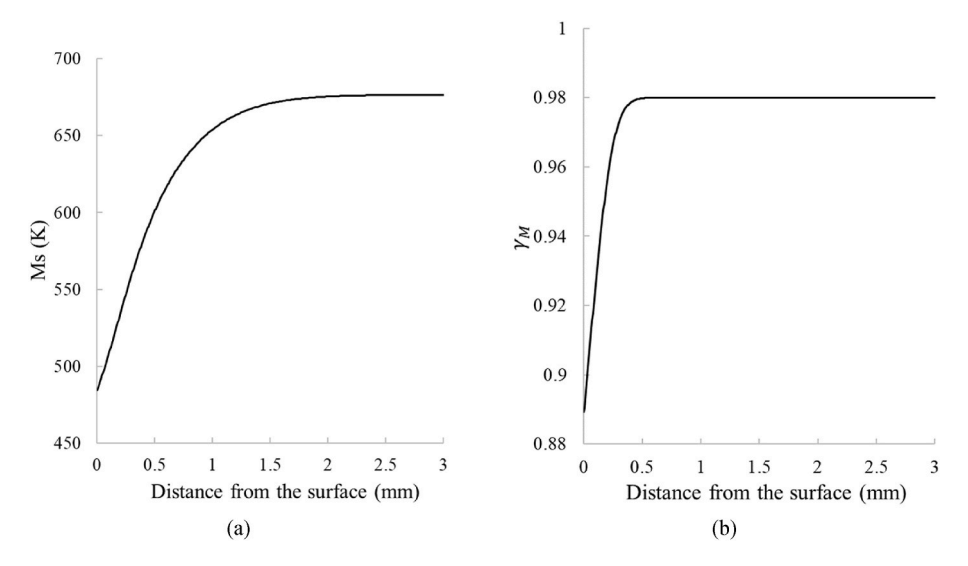


Fig. 7. (a)  $M_s$  and (b)  $\gamma_M$  evolutions as a function of the radius along the symmetry axis at the end of the quenching step.

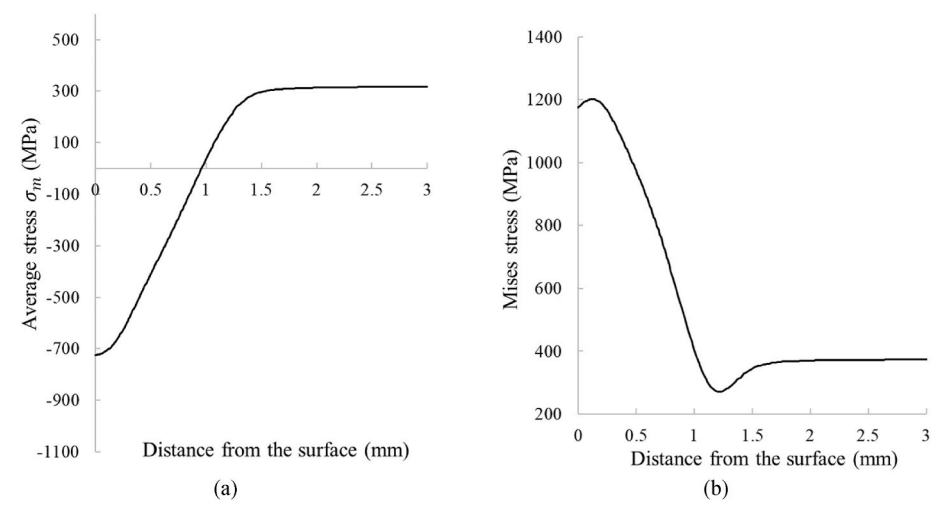


Fig. 8. Evolution of (a) The average hydrostatic pressure  $\sigma_m = -P_H$  and (b) The von Mises stress along the symmetry axis at the end the quenching step.

material properties, and last, results are given and commented. Two sets of computation are performed, considering, or not, the effect of hydrostatic pressure on carbon transport.

## 3.1. Configuration

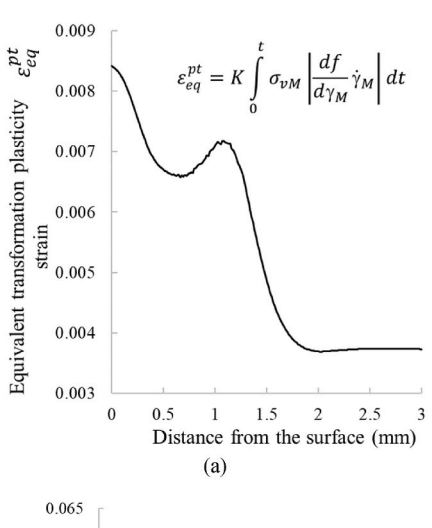
The configuration is a cylindrical sample made of 8620RH steel (see its composition in Table 1), depicted on Fig. 4a, loaded on all outer surfaces by both temperature and gaseous carbon-concentration.

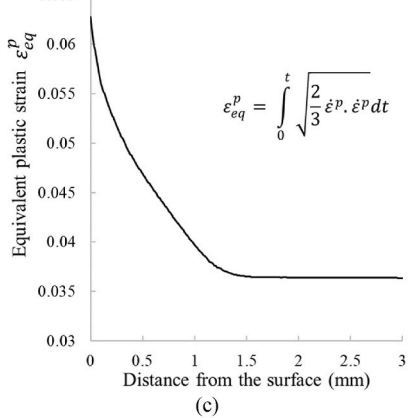
The loading scenario is divided into five steps:

- 1. Heating from 25 °C to 920 °C during 5 min;
- 2. Carburizing at  $T=920~^{\circ}\mathrm{C}$  during 200 min under a 0.9 wt% C atmosphere;
- 3. Carburizing at  $T=910~^{\circ}\mathrm{C}$  during 200 min under a 0.85 wt % C atmosphere:
- 4. Carburizing at  $T=820~^{\circ}\mathrm{C}$  during 150 min under a 0.75 wt % C atmosphere;
- 5. Air quenching to 25  $^{\circ}$ C during 3 min.

The problem is modelled in 3D (due to the way  $\nabla P_H$  is computed - see [36] for further details), meshed by full integration linear hexahedral elements C3D8T. A refined mesh was used near the surface and along the symmetry axis in order to better capture stress and strain gradients. In these regions, the element size was reduced to  $6\times 10^{-3}$  mm. In the rest of the domain, especially toward the revolution axis, the element size was progressively increased up to  $1.5\times 10^{-2}$  mm.

Initially,  $\gamma_M = O$  everywhere in the sample (i.e.,  $\gamma_{Ai} = 1$ ).





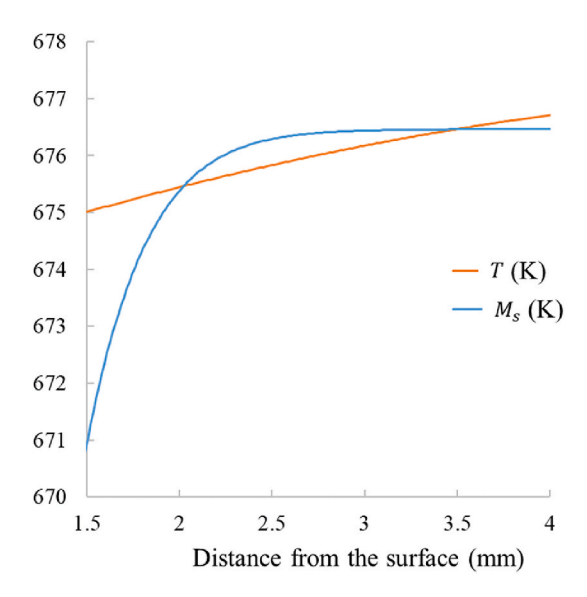
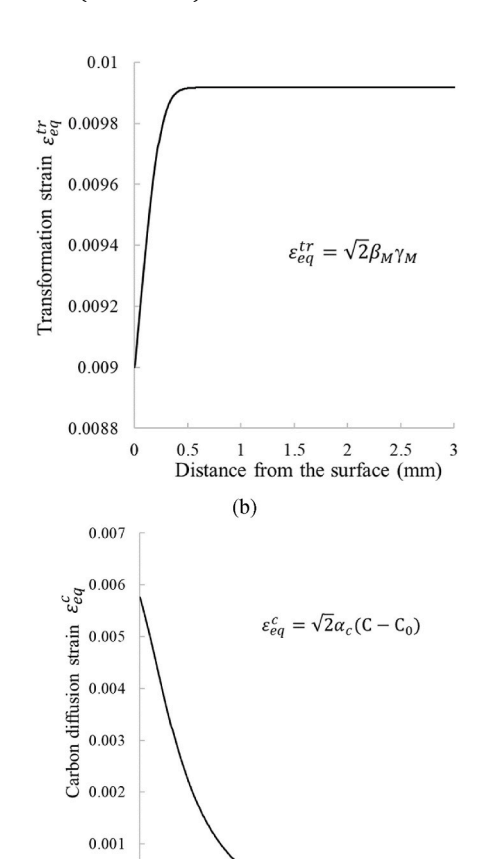


**Fig. 10.** Evolution of the martensite transformation temperature  $M_s$  and the temperature along the symmetry axis at t = 95s.

## 3.2. Material parameters

Temperature-dependent mechanical parameters were extracted from [35] for pure martensite and austenite, and fitted by polynomial functions (see Table 2).



Distance from the surface (mm)

(d)

Fig. 9. Variation along the symmetry axis of (a) The equivalent transformation plasticity  $\varepsilon_{eq}^{pt}$ , (b) The equivalent transformation strain  $\varepsilon_{eq}^{tr}$ , (c) The equivalent plastic strain  $\varepsilon_{eq}^{p}$  and (d) The equivalent carbon diffusion strain  $\varepsilon_{eq}^{c}$  in %.

0

Heat transfer parameters (thermal conductivity k, density  $\rho$  and specific heat  $C_p$ ) are provided in Table 3, from data extracted from [20]. As it was difficult to identify a polynomial function to fit these data satisfactorily, they have been used in a tabular way.

It is worth noting that the evolution of the heat transfer parameters with T are not monotonic. This is due to the metallurgical transformation occurring around 800  $^{\circ}$ C from BCC ferrite to FCC austenite. Thermal expansion for the martensitic an austenitic structure, volume and phase transformation coefficients have been obtained from [8]:

$$\begin{cases} \alpha_M = 1.43 \times 10^{-5} \text{ for martensite} \\ \alpha_A = 2.77 \times 10^{-5} \text{ for austenite} \\ \alpha_C = 0.0105 \\ \beta_M = 0.0101 \end{cases}$$
(19)

For non-pure phases, all parameters are computed based on the percentage of each phase: e.g.,  $\alpha = \gamma_M \alpha_M + (1 - \gamma_M) \alpha_A$ .

 $\alpha_{\rm C}$  (equation (19)) has been identified from the results provided in [8], in which the dilatation of the sample's diameter  $\Delta d/d$  is provided as a function of the temperature and the carbon content of the surrounding atmosphere. In Fig. 5 the  $\Delta d/d$  evolution from [8] and in the present study are compared, based on the inverse identification of  $\alpha_{\rm C}$ : as it can be observed, results are consistent with [8]. It is worth noting that, as temperature decreases to the ambient temperature (e.g., during step 5), the thermal strain becomes negligible compared to the dilatation induced by carbon atoms.

Equation (6) and Table 1 have been used to compute the diffusion coefficient D as a function of the carbon concertation C. The partial carbon molar volume  $V_c$  is set to  $3.9 \times 10^{-6}$  m<sup>3</sup>/mol [18]. The transformation plasticity coefficient K is set to  $2.5 \times 10^{-5}$  [35]. Last, the temperature  $M_s$  at which martensitic transformation begins and the material parameter  $A_M$  are computed using equations (10) and (11).

## 3.3. Results

A carburizing -quenching computation was performed without considering the impact of hydrostatic pressure on diffusion ( $V_c = 0$ , see equation (4)), the results of which are then discussed.

Then, hydrostatic pressure is accounted for in diffusion ( $V_c \neq 0$ ), which also has an impact on the boundary conditions.

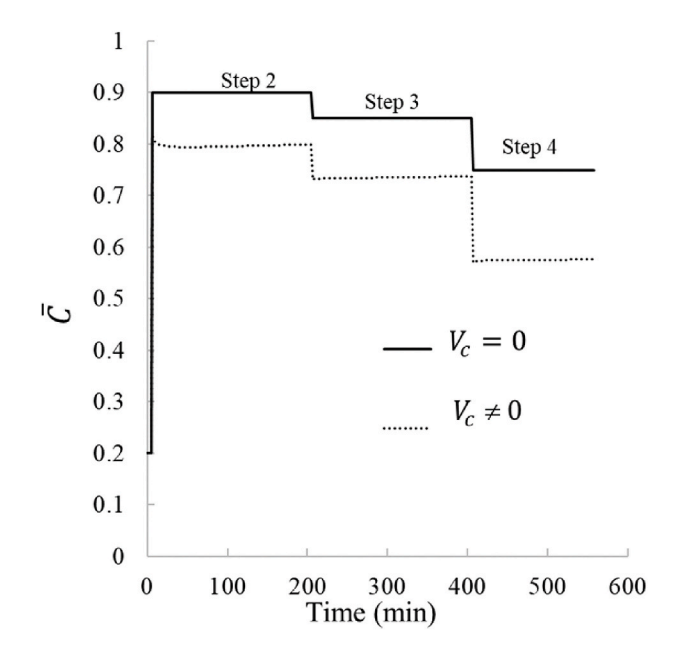


**Fig. 11.** Carbon-concentration boundary condition  $\overline{C}$  without (solid line) and with (dashed line)  $P_H$ .

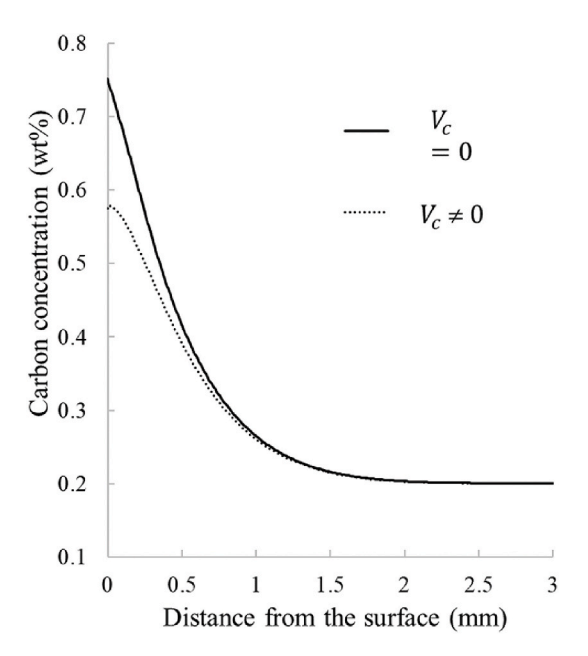


**Fig. 12.** Carbon-concentration evolution along the symmetry axis at the end of the diffusion process (step 4).

Unless stated, all results are plotted at the end of the quenching process (step 5), along the symmetry axis.

#### 3.3.1. Carburizing steps

Fig. 6a shows the diffusion profile at the end of each step under a carbon-rich atmosphere (steps 2–4).

It can be observed that carbon remains at the sample's surface (less than 1 mm deep for a radius equal to 6.35 mm), consistent with the low value of D at 900 °C. Step 4 shows no evolution of the diffusion profile, as the diffusion coefficient at 820 °C is too low (equal to  $9.29 \times 10^{-7}$  mm<sup>2</sup>/s when C is equal to 0.9 wt%). From these carbon profiles, the Vickers hardness HV can be estimated using the following relationship [8]

$$HV = 127 + 949C + 27Si + 11Mn + 8Ni + 16Cr + 21 \log V_M$$
 (20)

where  $V_M$  is a critical cooling rate for martensite, equal to 10 °C/s (concentrations in equation (20) are in mass.fr).

The equivalence with the HCR's hardness is set following [39].

$$HCR = \frac{100 \times HV - 14500}{HV + 223} \tag{21}$$

The HCR hardness prolife is plotted in Fig. 6b along the symmetry axis and compared with the one from [8]. If maximum values are the same (which is expected as the carbon boundary condition are the same in both studies), it can be observed that the carbon penetration in [8] is more important, i.e., the value of D used in [8] is probably greater than the one considered here. It is worth noting that this value has not been provided in [8], where it is only mentioned that it is temperature and carbon-concentration-dependent: this variation in D certainly has an influence on the identified  $\alpha_{\rm C}$  as well (see Fig. 5).

# 3.3.2. Quenching step

During the quenching step (step 5), the initially austenitic structure transforms into martensite, depending on both the carbon-concentration and the temperature. This process, assumed to be instantaneous as previously underlined (equation (9)), is controlled by the transformation temperature  $M_s$ , which is decreasing with C (see equation (11)).  $M_s$  and  $\gamma_M$  profiles along the symmetry axis of the sample are plotted in Fig. 7, at the end of the quenching step (step 5).

 $M_s$  increases from the surface of the sample to around 1 mm deep,

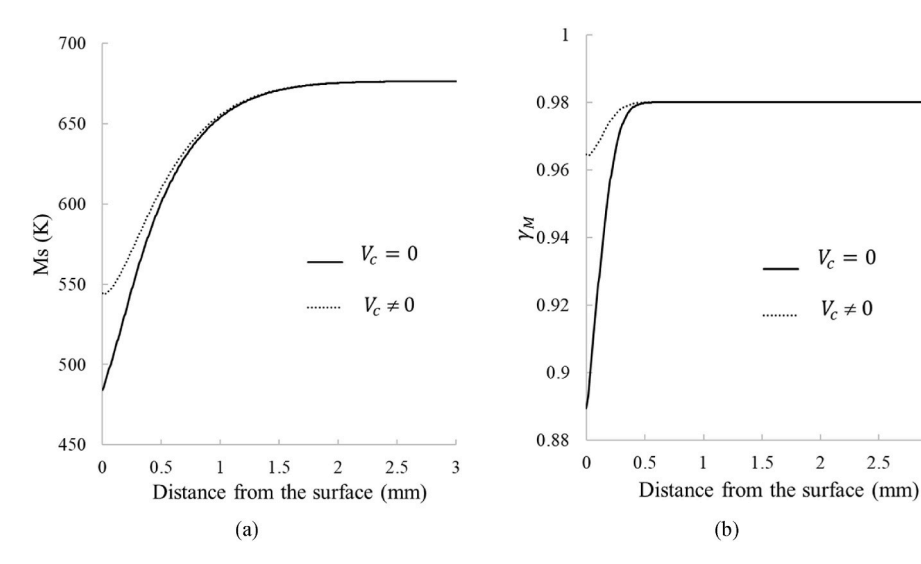


Fig. 13. (a)  $M_s$  and (b)  $\gamma_M$  as a function of the radius along the symmetry axis at the end of the quenching step.

from where it becomes constant, consistently with the carbon profile depicted in Fig. 6a. The martensite fraction  $\gamma_M$  is lower near the outer surface because the local decrease in  $M_s$  slows down the onset of the martensitic transformation.

#### 3.3.3. Mechanical fields at the end of the quenching process (step 5)

Fig. 8a shows the repartition of the average stress  $\sigma_m = -P_H$  along the symmetry axis. Compression can be observed below the sample surface (i.e. where carbon atoms have diffused), inducing a tensile stress elsewhere. There are two reasons for this behavior: firstly, volume expansion is greater in the martensite-rich core, which tends to expand during transformation. The surface, which is cooler, less transformed and thus mechanically more rigid, slows down this internal expansion. This blocking creates a state of compression on the surface and traction in the volume, which is consistent with observed tendencies (see, e.g., [12,14,19,35]). Secondly, dilatation linked to carbon diffusion also plays an important role, since it creates compression zones.

This compression is associated to a very high von Mises stress (Fig. 8b), reaching its maximal value close to the surface, due to strong transformation-induced incompatibilities and the coexistence of martensite and retained austenite, which generate significant deviatoric stress components. The martensitic transformation deforms the material unevenly and in specific directions, since it occurs locally - some areas transform before others. The surrounding material (still austenitic or already transformed) resists this deformation, creating internal stresses. It can be observed that, at depth, where the effects of cooling are less marked, residual stresses gradually decrease. This zone is generally characterized by low-amplitude stresses [12,14,19,35].

The evolution of stresses can be interpreted through the different strain contributions within the material:

- The equivalent transformation-induced plastic strain  $\varepsilon_{eq}^{pt}$  (Fig. 9a) exhibits a pronounced maximum near the surface, followed by a local peak around 1 mm in depth. The peak indicates the place where the beginning of the martensitic transformation takes place. During quenching, the temperature of the sample is not constant, but shows its maximum value at the axis of revolution. The martensitic transformation is triggered when the temperature becomes lower than  $M_s$ , which occurs at the peak after 100 s of quenching (see Fig. 10). This peak is linked to a low von Mises stress value (Fig. 8b).
- The equivalent transformation strain  $\varepsilon_{eq}^{tr}$  (Fig. 9b) is proportional to the martensite fraction (Fig. 7b). It is minimal at the surface, where retained austenite remains, and maximal in the core, where the

microstructure is predominantly martensitic. This induces additional mismatch with the less-transformed surface.

2.5

- ullet These gradients are accompanied by plasticity  $arepsilon_{eq}^p$ , which is pronounced near the surface and strongly correlated with the von Mises stress (Fig. 9c).
- ullet The equivalent carbon-induced strain  $arepsilon_{eq}^c$  reaches its maximum at the surface and gradually decreases toward the sample's center (Fig. 9d). This trend directly reflects the carbon-concentration profile, where local expansion at the surface is mechanically constrained by the geometry and less enriched regions, leading to compressive stresses.

## 3.3.4. Impact of hydrostatic pressure on diffusion

Hydrostatic pressure on carbon diffusion has two main consequences: first, the carbon flux is modified (equation (4)) and carbon atoms tend to diffuse faster through areas in expansion ( $P_H < 0$ ). Second, the carbon adsorption/absorption process is also modified: considering an instantaneous carbon adsorption/absorption reaction, the chemical potential equality between the gaseous carbon and the atom in solution is given by the following boundary condition for C [40,41]

$$\overline{C} = C_0 \exp \left[ -\frac{DV_c}{RT} P_H \right]$$
 (22)

in which  $C_0$  represents the carbon-concentration values in the neighboring atmosphere (0.9 %, 0.85 and 0.75 %). The evolution of  $\overline{C}$  is presented in Fig. 11 with or without accounting for the impact of  $P_H$  (i.e. considering respectively  $V_c \neq 0$  and  $V_c = 0$ ).

It is worth noting that equation (22) has not been implemented in the flowchart presented in Fig. 3, but computed using the previous  $P_H$ -free results (week coupling).

Fig. 12 shows the comparison of the carbon-concentration profiles along the symmetry axis with and without  $P_H$ , at the end of the diffusion process. It can be observed that the diffusion depth is not modified, but the level of  ${\cal C}$  at the sample surface is significantly lower.

The consequences on the quenching process are illustrated in Fig. 13, in which both  $M_s$  and  $\gamma_M$  evolution along the symmetry axis are plotted. Compared to the case without hydrostatic pressure,  $M_s$  starts from higher values at the surface, due to the lower carbon content, resulting from the hydrostatic compression that hinders carbon absorption in the sample. Consequently, the martensite fraction  $\gamma_M$  is also higher in this region, as the transformation is facilitated by the earlier intersection between temperature and  $M_s$  during cooling (which occurs at t = 80 s, at the same location than in the previous section).

The consequences on the mechanical fields and equivalent strains can be seen in Fig. 14, in which mechanical fields and strains evolution

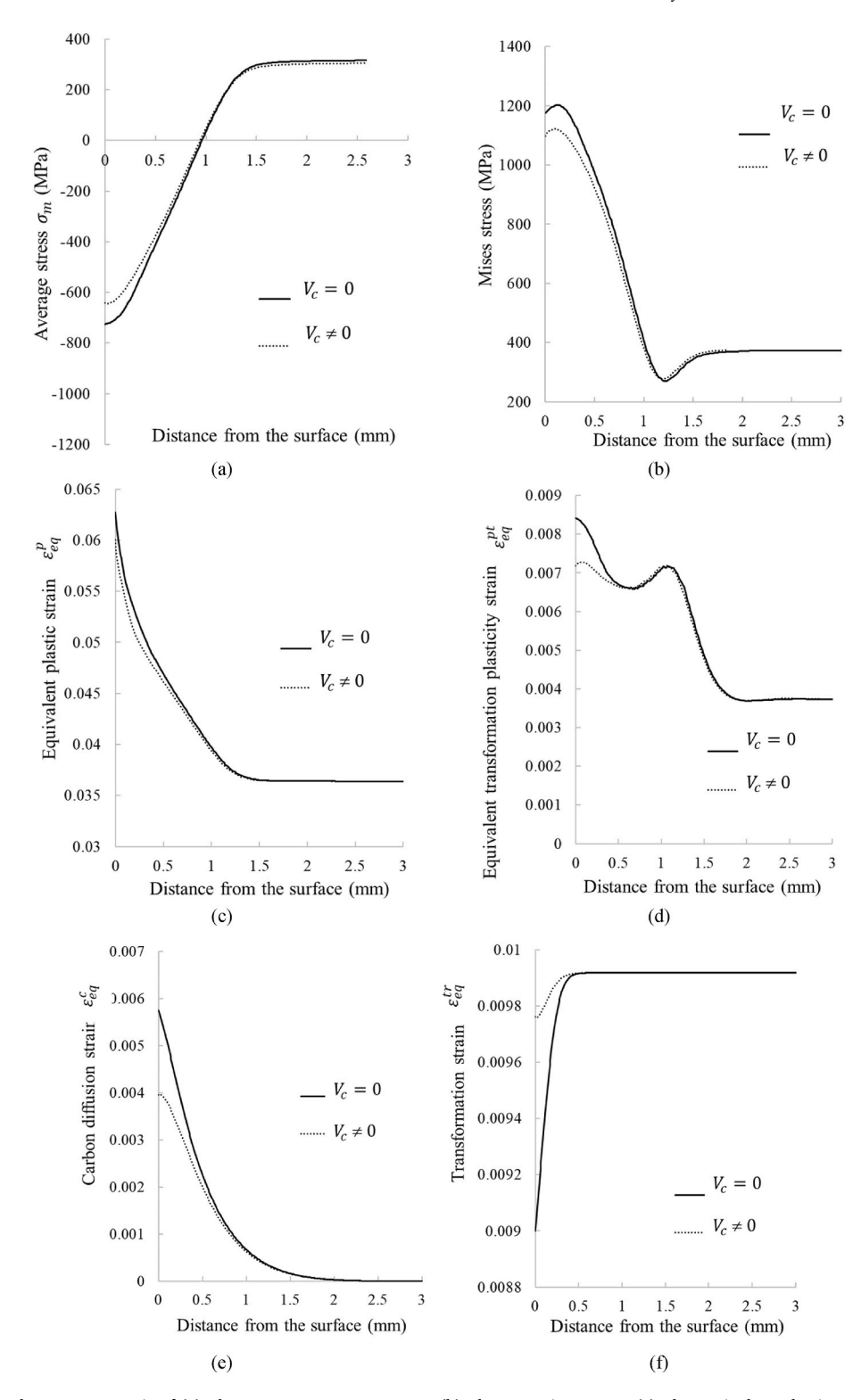


Fig. 14. Variation along the symmetry axis of (a) The average  $\sigma_m = -P_H$  stress, (b) The von Mises stress, (c) The equivalent plastic strain  $\varepsilon_{eq}^p$ , (d) The equivalent transformation plasticity strain  $\varepsilon_{eq}^{pt}$ , (e) The equivalent carbon diffusion strain  $\varepsilon_{eq}^c$  and (f) The equivalent transformation strain  $\varepsilon_{eq}^{tr}$  without (solid line) and with (dashed line)  $P_H$ .

along the symmetry axis are plotted at the end of the quenching step, and compared with the results without  $P_H$  (previous section).

Due to the increase in the martensitic fraction  $\gamma_M$  at the surface, the transformation differential is reduced, thus reducing the average compressive stresses  $\sigma_m$  at the surface (Fig. 14a). This attenuation is also reflected in von Mises stresses (Fig. 14b). On the deformation side,

diffusion deformation  $\varepsilon_{eq}^{\ c}$  directly follows the concentration profile, and clearly decreases with it (Fig. 14e). Transformation strain  $\varepsilon_{eq}^{\ tr}$  (Fig. 14f) increases at the surface, following the new distribution. At the same time, plastic transformation strain  $\varepsilon_{eq}^{\ pt}$  and plasticity strain  $\varepsilon_{eq}^{\ p}$  become more homogeneous (Fig. 14c and d), reflecting a reduction in internal mechanical gradients. Thus, hydrostatic pressure tends to reduce

internal heterogeneities and residual stress peaks, making processing more mechanically balanced.

It should be noted that the impact on  $P_H$  diffusion is limited to the diffusion steps (step 2–4), for which the temperature T is sufficiently high. As soon as quenching occurs, diffusion tends to become negligible.

#### 4. Conclusion

A model coupling heat transfer, mechanics, metallurgical change, and diffusion was implemented in the Abaqus finite element software to simulate the carburizing-quenching process. This implementation was achieved using user procedures, allowing for a coupled solution of the carbon diffusion process during the carburizing phases.

This model was then applied to a model configuration to illustrate the effect of stress and strain distribution on carburizing.

It was observed that, for the studied configuration, carbon penetrates only slightly, resulting in heterogeneous mechanical fields near the surface. In particular, a compression zone appears on the surface, associated with irreversible deformations related to the austenite-martensite phase change, for which a peak indicates the location

where the phase change begins during the quenching phase.

The impact of hydrostatic pressure is limited to the surface region and has no impact on the diffusion depth. The consequences in terms of deformation are also limited to the surface, and tends to reduce irreversible deformation gradients, and therefore stresses.

From an engineering perspective, this stress redistribution tends to slightly reduce the surface hardness, due to the attenuation of the carbon gradient and transformation intensity. Consequently, neglecting hydrostatic pressure may lead to a slight overestimation of surface hardness and residual stress peaks, especially in cases where strong phase transformations occur near the surface. This suggests that, while the overall impact remains localized, accounting for hydrostatic effects can improve the accuracy of predictions for surface integrity and mechanical performance.

#### Declaration of competing interest

The authors declare that they have no known competing financial interests or personal relationships that could have appeared to influence the work reported in this paper.

# **Appendix**

Carburizing-quenching finite element models

This table presents a summary comparison of the different modeling approaches presented in the literature, highlighting the phenomena considered.

It should be noted that this study stands out for its consideration of two terms related to carbon diffusion:

- diffusion-induced expansion;
- the impact of hydrostatic pressure on diffusion.

Reference	Transient Fick law	D(C, T)	$\nabla P_H$	$arepsilon^{tr}$	$arepsilon^{tp}$	$\varepsilon^T$	$\varepsilon^C$	Transient heat law	Heat source due to Phase transformation	Phase transformation	Mechanical behavior	Software
Zhong et al. [35]				X	X	X		X		X	Plasticity	Abaqus
Kim et al. [21]	X	X			X	X		X	X	X	Visco plasticity	Abaqus
Mukai et al. [5]				X	X	X		X	X	X	Plasticity	Cosmap
Ju D-Y et al. [22]				X	X	X		X	X	X	Visco plasticity	Cosmap
Li et al. [1]					X	X					Plasticity	Gid + Cosmap
Wang et al. [24]	X			X	X	X		X	X	X +		Cosmap
Lee et al. [7]	X	X								X		Abaqus+ Dante
Yaakoubi et al. [34]				X	X	X		X	X		Plasticity	Abaqus
Chen et al. [19]				X	X	X		X	X	X	Plasticity	Abaqus
Jiří et al. [30]	X											
Jung et al. [42]	X	X										Abaqus
Kim et al. [43]	X	X										Abaqus
Lee et al. [44]										X		Abaqus
Karabelchtchikova et al. [45]	X											Homemade
Qin et al. [14]	X	X		X	X	X		X	X	X	Plasticity	
Liu et al. [8]	X	X		X	X	X	X	X		$X^{++}$	Plasticity	Abaqus
Liu et al. [9]	X			X	X	X		X	X	X	Plasticity	Abaqus
Iżowski et al. [15]	X	X						X	X	X		Deform3d + Simufact Forming
Liu et al. [16]	X	X						X	X	X		Abaqus + Dante
Yan et al. [46]				X	X	X				X	Plasticity	Dante
Yang et al. [10]	X							X	X	X		Abaqus
Wang et al. [11]	X							X	X	X		CoSim
Li et al. [17]	X	X						X	X	X		Comsol
Rumony et al. [47]	X	X						X		X		Simufact

(continued on next page)

#### (continued)

Reference	Transient Fick law	D(C, T)	$\nabla P_H$	$arepsilon^{tr}$	$arepsilon^{tp}$	$\varepsilon^T$	$\varepsilon^C$	Transient heat law	Heat source due to Phase transformation	Phase transformation	Mechanical behavior	Software
Li et al. [48]	X							X		X		Dante
Yingtao et al. [49]	X	X										Abaqus
Yuan et al. [25]	X	X								X +		Deform
Shao et al. [20]	X	X		X	X	X		X	X	$X^{++}$	Plasticity (no details)	
Wang et al. [18]	X	X	X					X			X	Deform
Teixeira et al. [23]				X	X	X				X	Plasticity	
Wołowiec-Korecka et al. [13] (review)	X	X		X	X	X		X	X	X	Plasticity	
Denis et al. [12] (review)	X			X	X	X		X	X	X	Plasticity	
Wijnen et al. [28]			X	X	X	X		X		X	Plasticity	Abaqus
This work	X	X	X	X	X	X	X	X		X	plasticity	Abaqus

<sup>+</sup> stress impact on phase transformation.

#### References

- [1] Li X, Ju D, Cao J, Wang S, Chen Y, He F, et al. Effect of transformation plasticity on gear distortion and residual stresses in carburizing quenching simulation. Coatings 2021;11:1224. https://doi.org/10.3390/coatings11101224.
- [2] Wang H, Wang B, Wang Z, Tian Y, Misra RDK. Optimizing the low-pressure carburizing process of 16Cr3NiWMoVNbE gear steel. J Mater Sci Technol 2019;35: 1218–27. https://doi.org/10.1016/j.jmst.2019.02.001.
- [3] Stratton PF, Bruce S, Cheetham V. Low-pressure carburizing systems: a review of current technology. BHM Berg- Hüttenmännische Monatsh 2006;151:451–6. https://doi.org/10.1007/BF03165206.
- [4] Marray T. Carbonitruration basse pression d'aciers et de pièces obtenues par la technologie MIM. Ecole nationale supérieure d'arts et métiers - ENSAM; 2012. PhD thesis (in French), https://pastel.archives-ouvertes.fr/pastel-00840622. [Accessed 20 October 2022].
- [5] Mukai R, Ju D-Y. Simulation of carburizing-quenching of a gear. Effect of carbon content on residual stresses and distortion. J Phys IV - Proc 2004;120:489–97. https://doi.org/10.1051/jp4:2004120056.
- [6] Soleimani M, Kalhor A, Mirzadeh H. Transformation-induced plasticity (TRIP) in advanced steels: a review. Mater Sci Eng A 2020;795:140023. https://doi.org/ 10.1016/j.msea.2020.140023.
- [7] Lee S-J, Matlock DK, Van Tyne CJ. Comparison of two finite element simulation codes used to model the carburizing of steel. Comput Mater Sci 2013;68:47–54. https://doi.org/10.1016/j.commatsci.2012.10.007.
- [8] Liu H, Hu X, Tang J, He Y, Shao W, Sun B, et al. A novel method for predicting carburizing and quenching deformation of the gear with the mandrel based on carburizing expansion strain and dynamic thermal boundary conditions of quenching. Surf Coat Technol 2024;494:131377. https://doi.org/10.1016/j. surfcoat.2024.131377.
- [9] Liu H, Tang J, Liu C, Liu Y, Jiang W, Sun B. Understanding the distinction between quenching and carburizing quenching stress field: evolution mechanism of quenching stress field influenced by carbon content in low-carbon alloy steel. Surf Coat Technol 2024;489:131112. https://doi.org/10.1016/j.surfcoat.2024.131112.
- [10] Yang S, Chen W, Liang R. Residual stresses in gear form grinding by considering carburizing heat treatment: multi-field coupled numerical simulation and experimental verification. Int J Adv Manuf Technol 2024;131:4981–99. https:// doi.org/10.1007/s00170-024-13293-5.
- [11] Wang H, Wang J, Xu J, Gu J, Guo Z, Yu N. Multi-field coupling simulation of vacuum carburizing and high-pressure gas quenching process. Heat Treat Surf Eng 2022;4:54–63. https://doi.org/10.1080/25787616.2022.2073051.
- [12] Denis S, Archambault P, Gautier E, Simon A, Beck G. Prediction of residual stress and distortion of ferrous and non-ferrous metals: current status and future developments. J Mater Eng Perform 2002;11:92–102. https://doi.org/10.1007/ s11665-002-0014-2.
- [13] Wołowiec-Korecka E. Modeling methods for gas quenching, low-pressure carburizing and low-pressure nitriding. Eng Struct 2018;177:489–505. https://doi. org/10.1016/j.engstruct.2018.10.003.
- [14] Qin S, Ma H, Wang L. Stress field simulation and its experimental verification of carburizing-quenching process performed on 18CrNiMo7-6 steel. Mater Sci 2023; 29:167–75. https://doi.org/10.5755/j02.ms.30932.
- [15] Izowski B, Wojtyczka A, Motyka M. Numerical simulation of low-pressure carburizing and gas quenching for pyrowear 53 steel. Metals 2023;13:371. https://doi.org/10.3390/met13020371.
- [16] Liu Y, Tang J, Liu H, Jiang W. The influence of carbon content gradient and carbide precipitation on the microstructure evolution during carburizing-quenchingtempering of 20MnCr5 bevel gear. Surf Coat Technol 2024;494:131387. https:// doi.org/10.1016/i.surfcoat.2024.131387.
- [17] Li J, Xu Y, Liu Y, He H. Investigation of non-uniformity of temperature distribution and phase transformation in spiral bevel gears during carburizing and quenching. J Mater Sci 2024;59:609–30. https://doi.org/10.1007/s10853-023-09182-z.

- [18] Wang Y, Gong J. Measurement and calculation of carbon concentration and diffusion-induced stress in stainless steel after low temperature gas carburizing. Acta Met Sin 2014;50:409–14. https://doi.org/10.3724/SP.J.1037.2013.00537.
- [19] Chen J, Zuo Z, Zhou S, Wang X, Chen Y, Ling G. Study on the compressive stress retention in quenched cam of 100Cr6 steel based on coupled thermomechanical and metallurgical modeling. Materials 2021;14:5912. https://doi.org/10.3390/ ma14205912.
- [20] Shao W, Yi M, Tang J, Sun S. Prediction and minimization of the heat treatment induced distortion in 8620H steel gear: simulation and experimental verification. Chin J Mech Eng 2022;35:126. https://doi.org/10.1186/s10033-022-00802-4.
- [21] Kim D-W, Cho H-H, Lee W-B, Cho KT, Cho Y-G, Kim S-J, et al. A finite element simulation for carburizing heat treatment of automotive gear ring incorporating transformation plasticity. Mater Amp Des 2016;99:243. https://doi.org/10.1016/j. matdes.2016.03.047.
- [22] Ju D-Y. Residual stress and distortion: designing for control of. Encycl. Iron steel their alloys online version. CRC Press; 2016.
- [23] Teixeira J, Jeyabalan K, Geandier G, Dulcy J, Denand B, Chini M-R, et al. In situ HEXRD experimental study and prediction of microstructures and internal stresses during heat treatment of carburized and carbonitrided low-alloyed steels. Acta Mater 2024;275:120065. https://doi.org/10.1016/j.actamat.2024.120065.
- [24] Wang J, Yang S, Li J, Ju D, Li X, He F, et al. Mathematical simulation and experimental verification of carburizing quenching process based on multi-field coupling. Coatings 2021;11:1132. https://doi.org/10.3390/coatings11091132.
- [25] Yuan Y, Zhang Q, Xue Y, Jiang Y, Liu K, Shen X, et al. Effects of high temperature tempering on microstructure and hardness distribution on 18Cr2Ni4WA alloy steel heavy-duty gears: numerical simulation and experiments. J Phys Conf Ser 2023; 2549:012028. https://doi.org/10.1088/1742-6596/2549/1/012028.
- [26] Dassault Systèmes Simulia Corp. ABAQUS/Standard user's manual. United States. 2022.
- [27] Dassault Systèmes Simulia Corp. ABAQUS user subroutines reference guide. United States. 2022.
- [28] Wijnen J, Parker J, Gagliano M, Martínez-Pañeda E. A computational framework to predict weld integrity and microstructural heterogeneity: application to hydrogen transmission. Mater Des 2025;249:113533. https://doi.org/10.1016/j. matles 2024 113533
- [29] Li JCM, Oriani RA, Darken LS. The thermodynamics of stressed solids. Z Für Phys Chem 1966;49:271–90. https://doi.org/10.1524/zpch.1966.49.3 5.271.
- [30] Jiří M, Iva N, Pavel Š. Calculation of carbon diffusion for cementation of gear wheels. MM Publ; 2018. p. 2441–50. https://doi.org/10.17973/MMSJ.2018\_10 2018.26
- [31] Lee S-J, Matlock DK, Van Tyne CJ. An empirical model for carbon diffusion in austenite incorporating alloying element effects. ISIJ Int 2011;51:1903–11. https://doi.org/10.2355/isiiinternational.51.1903.
- [32] Koistinen DP, Marburger RE. A general equation prescribing the extent of the austenite-martensite transformation in pure iron-carbon alloys and plain carbon steels. Acta Metall 1959;7:59–60. https://doi.org/10.1016/0001-6160(59)90170-1
- [33] Mazur J. Lattice parameters of martensite and of austenite. Nature 1950;166:828. https://doi.org/10.1038/166828a0. 828.
- [34] Yaakoubi M, Kchaou M, Fakhreddine D. Simulation of the thermomechanical and metallurgical behavior of steels by using ABAQUS software. Comput Mater Sci 2013;68:297–306. https://doi.org/10.1016/j.commatsci.2012.10.001.
- [35] Zhong H, Wang Z, Gan J, Wang X, Yang Y, He J, et al. Numerical simulation of martensitic transformation plasticity of 42CrMo steel based on spot continual induction hardening model. Surf Coat Technol 2020;385:125428. https://doi.org/ 10.1016/j.surfcoat.2020.125428.
- [36] Charles Y, Nguyen HT, Gaspérini M. FE simulation of the influence of plastic strain on hydrogen distribution during an U-bend test. Int J Mech Sci 2017;120:214–24. https://doi.org/10.1016/j.ijmecsci.2016.11.017.

<sup>&</sup>lt;sup>++</sup> kinetic phase transformation, For viscoplasticity, a viscous strain is included as well.

- [37] Vasikaran E, Charles Y, Gilormini P. Implementation of a reaction-diffusion process in the Abaqus finite element software. Mec Ind 2020;21:508. https://doi.org/ 10.1051/meca/2020010.
- [38] Bian S, Mougenot J, Charles Y, Bonnin X, Wauters T, Pitts R. Hydrogen retention in ITER's Diagnostic first wall submitted to cyclic thermomechanical loadings. Procedia Struct Integr 2022;42:172–9. https://doi.org/10.1016/j. prostr.2022.12.021.
- [39] Qvarnström H. Technical note: a mathematical formula for transformation between the steel hardness scales of rockwell C and vickers. J Heat Treat 1989;7:65–7. https://doi.org/10.1007/BF02833189.
- [40] Charles Y, Nguyen HT, Gaspérini M. Comparison of hydrogen transport through pre-deformed synthetic polycrystals and homogeneous samples by finite element analysis. Int J Hydrogen Energy 2017;42:20336–50. https://doi.org/10.1016/j. ijhydene.2017.06.016.
- [41] Martínez-Pañeda E, Díaz A, Wright L, Turnbull A. Generalised boundary conditions for hydrogen transport at crack tips. Corros Sci 2020;173:108698. https://doi.org/ 10.1016/j.corsci.2020.108698.
- [42] Jung M, Oh S, Lee Y-K. Predictive model for the carbon concentration profile of vacuum carburized steels with acetylene. Met Mater Int 2009;15:971–5. https:// doi.org/10.1007/s12540-009-0971-1.

- [43] Kim D-W, Cho Y-G, Cho H-H, Kim S-H, Lee W-B, Lee M-G, et al. A numerical model for vacuum carburization of an automotive gear ring. Met Mater Int 2011;17: 885–90. https://doi.org/10.1007/s12540-011-6004-x.
- [44] Lee S-J, Van Tyne CJ. A kinetics model for martensite transformation in plain carbon and low-alloyed steels. Metall Mater Trans A 2012;43:422–7. https://doi. org/10.1007/s11661-011-0872-z.
- [45] Karabelchtchikova O, Sisson RD. Carbon diffusion in steels: a numerical analysis based on direct integration of the flux. J Phase Equilibria Diffus 2006;27:598–604. https://doi.org/10.1007/BF02736561.
- [46] Yan Y, Xue Y, Yu W, Liu K, Wang M, Wang X, et al. Predictions and experiments on the distortion of the 20Cr2Ni4A C-ring during carburizing and quenching process. Materials 2022;15:4345. https://doi.org/10.3390/ma15124345.
- [47] Rumony A, Szlancsik A, Kovács D. Verification of the simulated carburizing process in different bore sizes. Coatings 2023;13:1019. https://doi.org/10.3390/ coatings13061019.
- [48] Li Z, Ferguson BL, Lee E, Habean S, Meyer J. Sources of heat treatment distortion and approaches for distortion reduction during quench hardening process. ASM International; 2024. p. 132–8. https://doi.org/10.31399/asm.cp.ifhtse2024p0132.
- [49] Yingtao Z, Zirong T, Lei H, Mahdipanah MH, Yanjie W. Real-time prediction method of carbon concentration in carburized steel based on a BP neural network. Heat Treat Surf Eng 2024;6:2350184. https://doi.org/10.1080/ 25787616.2024.2350184.